ADVANCED HEALTHCARE MATERIALS
www.advhealthmat.de

Multiscale Modeling of Magnetoelectric Nanoparticles for the Analysis of Spatially Selective Neural Stimulation

*Prachi Kumari, Hannah Wunderlich, Aleksandra Milojkovic, Jorge Estudillo López, Arianna Fossati, Ali Jahanshahi, and Kristen Kozielski**

The growing field of nanoscale neural stimulators offers a potential alternative to larger scale electrodes for brain stimulation. Nanoelectrodes made of magnetoelectric nanoparticles (MENPs) can provide an alternative to invasive electrodes for brain stimulation via magnetic-to-electric signal transduction. However, the magnetoelectric effect is a complex phenomenon and challenging to probe experimentally. Consequently, quantifying the stimulation voltage provided by MENPs is difficult, hindering precise regulation and control of neural stimulation and limiting their practical implementation as wireless nanoelectrodes. The work herein develops an approach to determine the stimulation voltage for MENPs in a finite element analysis (FEA) model. This model is informed by atomistic material properties from ab initio Density Functional Theory (DFT) calculations and supplemented by experimentally obtainable nanoscale parameters. This process overcomes the need for experimentally inaccessible characteristics for magnetoelectricity, and offers insights into the effect of the more manageable variables, such as the driving magnetic field. The model's voltage is compared to in vivo experimental data to assess its validity. With this, a predictable and controllable stimulation is simulated by MENPs, computationally substantiating their spatial selectivity. This work proposes a generalizable and accessible method for evaluating the stimulation capability of magnetoelectric nanostructures, facilitating their realization as wireless neural stimulators in the future.

1. Introduction

Neural devices can diagnose and treat neurological disorders, enhance our understanding of the brain, and improve the overall quality of healthcare in the nervous system. In recent years, nanoscale neurostimulators have emerged as a solution to overcome the risks of traditional invasive stimulation devices.[1] Nanoscale stimulators interact with neural tissues via various cellular or molecular mechanisms and have the potential to provide wireless and minimally invasive neural therapy.[2–4] One such promising tool as a wireless, nanoscale neural stimulator is based on the principle of magnetoelectricity.[5]

Magnetoelectricity can be harnessed either directly from multiferroic materials, or indirectly via strain coupling of a magnetostrictive and piezoelectric material. In the latter case, a common interface between the two transmits the stress generated in the magnetostrictive phase to the piezoelectric phase following exposure to an external magnetic field (input) to create an electric stimulation (output) for neurons as shown

P. Kumari, H. Wunderlich, A. Milojkovic, J. E. López, K. Kozielski
Professorship of Neuroengineering Materials
School of Computation, Information and Technology
Technical University of Munich
80333 Munich, Germany
E-mail: kristen.kozielski@tum.de

A. Fossati
Department of Electronics and Information
Politecnico di Milano
Milano 20133, Italy

A. Jahanshahi
Department of Neurosurgery
Maastricht University Medical Center
Maastricht 6229, Netherlands

A. Jahanshahi
Netherlands Institute for Neuroscience
Royal Netherlands Academy of Arts and Sciences
Amsterdam 1105, Netherlands

K. Kozielski
Munich Institute of Biomedical Engineering
Technical University of Munich
85748 Garching, Germany

K. Kozielski
Munich Institute of Robotics and Machine Intelligence
Technical University of Munich
80992 Munich, Germany

The ORCID identification number(s) for the author(s) of this article can be found under https://doi.org/10.1002/adhm.202302871

© 2024 The Authors. Advanced Healthcare Materials published by Wiley-VCH GmbH. This is an open access article under the terms of the Creative Commons Attribution License, which permits use, distribution and reproduction in any medium, provided the original work is properly cited.

DOI: 10.1002/adhm.202302871

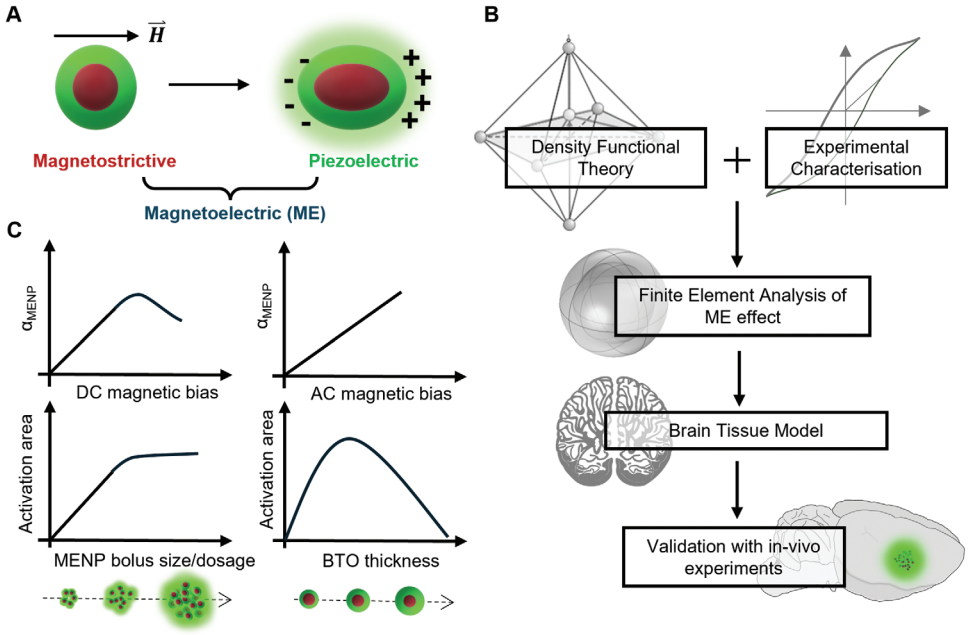

Figure 1. A) Working principle of magnetoelectric nanoparticles (MENPs) based on magnetostrictive and piezoelectric phases coupled via a common interface. B) Workflow designed to determine neuromodulatory capability of MENPs. C) Hypothesized correlation of tissue activation via MENPs based on varying input magnetic field and nanoparticle injection parameters.

in **Figure** 1A. In order to quantify the driving input to output, consistent work has been done to formulate the magnetoelectric co-efficient (α) for different types of connectivity between the magnetostrictive and piezoelectric phases.[6–8] Much of this work has been conducted for laminates and composites using effective medium theories or phase-field modeling. However, an emerging approach for leveraging magnetoelectricity in neuroengineering has been in the form of core-shell magnetoelectric nanoparticles (MENPs).[9,10]

Research has shown that MENPs can remotely evoke neuronal responses even in deep brain regions.[11] The use of core-shell nanoparticles has several advantages, such as an operational scale comparable to neural structures, the potential to cross the blood-brain barrier, and offers the possibility of surface coatings for better biocompatibility.

Currently, the precise control and influence of neural circuits through the stimulation voltage (output) provided by MENPs presents a challenge, with limited studies reporting or mapping the magnetoelectric coefficient (α_{MENP}).[12] This problem arises because magnetoelectric coefficient (α_{MENP}) is a function of intrinsic material parameters of the constituent phases, such as magnetostrictive constants, elastic constants, and spontaneous polarization, among others, which are difficult to directly measure experimentally. Furthermore, intrinsic material parameters are influenced by complex structural characteristics ranging from magneto-crystalline anisotropy, domain distribution, and domain wall motion of the phases.[13] Other factors, such as lattice mismatch and the presence of point defects, further contribute to the complexity.[14] Consequently, accurate control and manipulation of the intrinsic material parameters becomes a significant obstacle, especially when employing chemical synthesis routes to produce scale-able, significant quantities of polycrystalline MENPs.

The challenges associated with predicting and evaluating the stimulation voltage output of MENPs are multifaceted. An improved understanding of the interplay between the intrinsic material parameters and the resulting ME response is essential. Overcoming these challenges will contribute to developing MENPs as a precise and controllable tool for influencing neural circuits. In this work, these issues have been addressed and a generalizable method for determining the neuromodulatory capabilities of untethered nanoscale neural stimulators has been proposed as outlined in Figure 1B.

For the first time the feasibility of a multi-scale approach by considering the case of $CoFe_2O_4$ (CFO)-$BaTiO_3$ (BTO) core-shell MENPs.[5] has been conducted. This involves combining ab initio calculations based on Density Functional Theory (DFT) for atomistic level intrinsic properties, and simple experimental techniques such as X-ray Diffraction (XRD) for other easily measurable material properties. The calculated and measured material properties are then transferred to a Finite Element Analysis (FEA) model to study the physical phenomena of magnetostriction and piezoelectricity on which the MENPs operates. Further analysis of the α_{MENP} as a function of the applied magnetic field and shell thickness of the outer piezoelectric layer has been conducted. Finally, the model's output is validated by comparing it with in vivo experimentally measured neurostimulation data using a magnetic field generated by a Helmholtz coil as the stimulation source (220 mT DC, 6 mT AC at 140 Hz, 2.25 A). This also allows us to study the effects of the more controllable aspects of the MENPs based nanoelectrodes, paving a way for a more precise control over the generated stimulation voltage. Moreover, by

© 2024 The Authors. Advanced Healthcare Materials published by Wiley-VCH GmbH

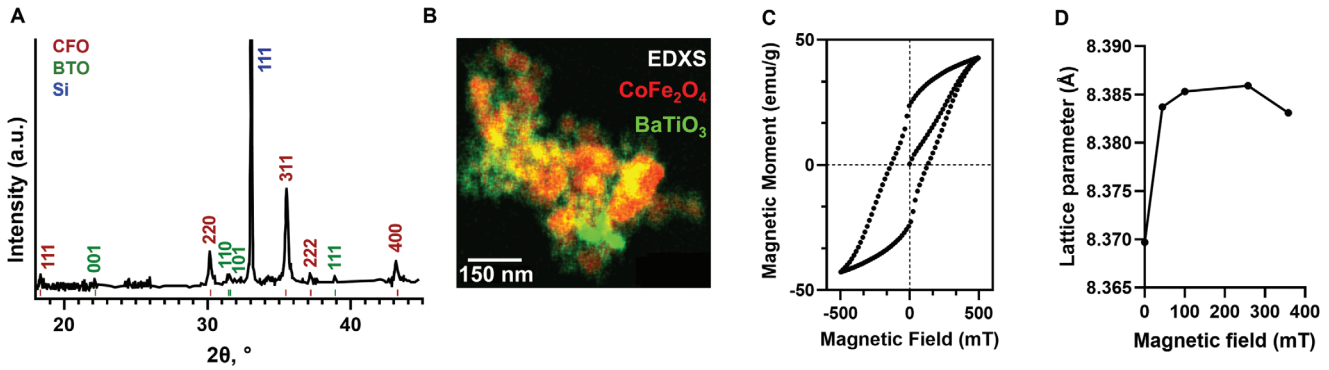

Figure 2. A) XRD of MENPs to confirm the tetragonal structure of $BaTiO_3$ (BTO) and cubic phase of $CoFe_2O_4$ (CFO). B) EDXS map of a magnetoelectric nanoparticle exhibits coupling between the magnetostrictive (CFO) and piezoelectric (BTO) phase. C) B-H curve for CFO nanoparticles. D) Change in lattice parameter of CFO as a function of DC magnetic bias as a measure of the particle's magnetostrictive response.

using this multi-scale methodology, the ability of superior spatial selectivity targeted to specific regions can be proven (Figure 1C).

In summary, this study unites diverse methodologies using a combination of simulation, modeling, and experimental verification. By bridging the gap between theoretical underpinnings and experimental reality, it offers a robust foundation for the development of advanced neural stimulation techniques and multiplexing in the future.

2. Results

2.1. Synthesis of MENPs and Determination of Material Properties

MENPs were synthesized using commercially available CFO nanoparticles as the starting core structure, and sol–gel synthesis for growth of the BTO shell. XRD was used to determine the crystallographic properties of the synthesize MENPs provided in **Figure** 2A. These patterns showcased the prominent peak indicative of the intended cubic phase of $CoFe_2O_4$. A discernible peak emerged at $2\theta = 31.5°$, aligning precisely with the characteristic signal of the tetragonal $BaTiO_3$ (BTO) phase.

The morphology of the synthesized MENPs was confirmed with High-angle Annular Dark-Field Scanning Transmission Electron Microscopy (HAADF-STEM) imagery (Figure S1, Supporting Information) and through Energy-Dispersive X-ray Spectroscopy (EDXS) given in Figure 2B, provided evidence of the average chemical composition to be $Co_{13\pm1.0}$ $Fe_{27.9\pm1.0}$ $Ba_{2.0\pm0.2}$ $Ti_{1.8\pm0.2}$ $O_{54.4\pm2.0}$ demonstrating within the error bars, the formation of $Co_{13.9}Fe_{27.9}O_{48.4}$-$Ba_{2.0}Ti_{1.8}O_6 \approx CoFe_2O_4$-$BaTiO_3$ MENPs. CFO and BTO are observed sharing a common interface and are located at each other's boundaries, demonstrating a successful coupling via a common interface.

CFO nanoparticles were measured via Vibrating Sample Magnetometer (VSM) and the magnetic moment as a function of applied magnetic field for CFO core yielded a typical hysteresis loop (Figure 2C). The saturation magnetization was 228.415 kAm^{-1} and the squareness ratio was 0.56. The initial magnetic susceptibility obtained at the beginning of the magnetization loop gave us the initial magnetic susceptibility of 0.746 (unitless).

Next, the magnetostriction of the core was measured using XRD to measure the CFO lattice parameters under an applied magnetic field. In the absence of any magnetic field, the lattice length was 8.369 $A°$ (l) from which a density of 5.32 gcm^{-3} was calculated using a molecular weight (M_w) of 234.63 $gmol^{-1}$.[15] The saturation magnetostriction was calculated as the average of $\frac{\delta l}{l}$ (Figure 2D).

After measuring the macro response of CFO core to an applied magnetic field, the elastic properties of the two phases were calculated to understand the effect of strain transfer. For this ab initio Density Functional Theory (DFT) calculations were performed starting with the crystal structure of CFO corresponding to a cubic inverse spinel structure and a lattice constant corresponding to the lattice parameter recorded by XRD was used (**Figure** 3A). For determination of the optimization parameters such as the k-point grid and kinetic energy cut-off, the crystal symmetry $Fd\bar{3}m$ (227) was used to specify the Wyckoff positions of Co, Fe, and O atoms. This ensures a low computational demand.

To reach the system energy minima, a 14-atom unit cell is used with a stable AB_2O_4 structure with a 2:1 distribution between Fe and Co. The unit cell is allowed to relax to its lowest energy position, where only the atomic positions are allowed to change while keeping the cell parameters constant. In lieu of complex experimental measurements to determine cation distribution in the tetrahedral and octahedral sites, an inverse spinel structure can be inferred based on the lattice parameter and AB_2X_4 structure confirmation by EDXS. Furthermore, annealing temperatures greatly influence the occupations at these sites with an unclear empirical trend. However, for annealing temperatures above 1073 K, a degree of inversion higher than 0.75 has been reported for CFO.[16,17]

A cross-verification between the computed crystal structure and CFO nanoparticles can be done by comparing the magnetic moment from atomistic calculations (Bohr magneton, μ_B) and saturation magnetisation (M_s) from the BH curve. Experimentally, the magnetic moment (η_b) was determined as 2.54 $\mu_B \approx 3\mu_B$ using the following formula:[18]

$$\eta_b = \frac{M_w \times M_s}{5585} \quad (1)$$

Theoretically, to determine the magnetic moment, a simplified generalized gradient approximation (GGA) with a Hubbard correction for on-site Coulomb repulsion energy (U) was

© 2024 The Authors. Advanced Healthcare Materials published by Wiley-VCH GmbH

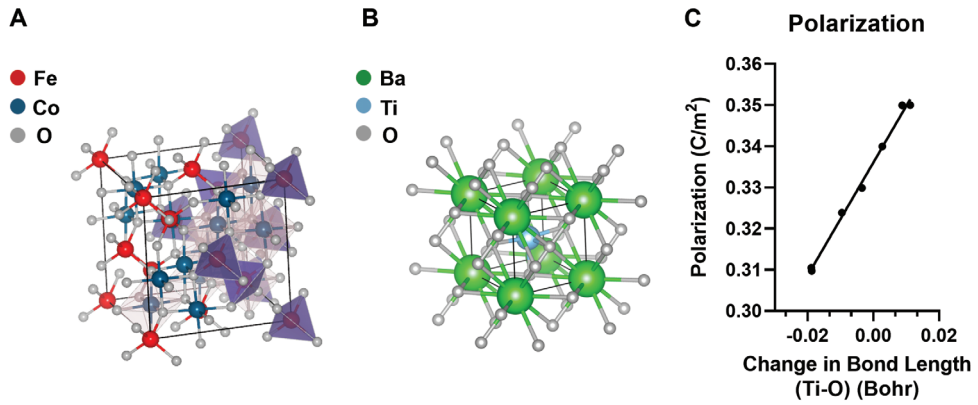

Figure 3. A) Conventional unit cell corresponding to a symmetric cell for inverse spinel CFO corresponding to Crystallography Open Database (COD) 1533163. B) Crystal structure of BTO used for atomistic modeling as per COD 1507756. C) Polarization versus change in bond length for BTO, the slope of which yields the polarization constant as 0.33 Cm^{-2}.

implemented as CFO is a strongly correlated structure.[19,20] The U value for both Co and Fe was set at 1.65 eV with a starting magnetization of 0.1 in the z-direction with no correction to the exchange interaction parameter (J). This gives us a total magnetization of 3.12 $\mu_B \approx 3\mu_B$.[21]

Following verification of the correct magnetic structure, an automatic workflow (*thermo_pw.x* routine) changed systematically the atomic positions and performed Self-Consistent Calculations (SCF) with ionic relaxation to generate the elastic constant as reported in **Table 1** and comparable to experimental values.[22,23]

Similarly, for BTO, we started with the convergence of parameters for SCF calculations with respect to the total energy of the system and used them for structural optimizations with initial atomistic position for Ba, Ti, and O from COD 1507756 (Figure 3B). The bulk modulus, calculated by the Murnaghan equation of state, yielded 129.19 GPa, which agreed with experimental and theoretical range reported in literature.[24,25] The elastic constants are calculated similarly to CFO by distorting the lattice but keeping the $\frac{c}{a}$ ratio constant. The values are reported in **Table 2**.

For the Berry phase calculation for BTO, the Ti and Ba atoms are moved such that it effectively corresponded to the application of out-of-plane compressive and tensile strain (ϵ_{33}) when the Ti ion's fractional coordinates are raised and lowered, respectively. As the compressive strain ϵ_{33} moves the Ti atom from its equilibrium position, forcing it into a cubic state, the polarization decreases, as seen in Figure 3C. The piezoelectric constant (d_{33}) was 159.58 pC/N and spontaneous polarization (P_s) from the linear fit was 0.33 Cm^{-2}.

Table 1. Properties of $CoFe_2O_4$ (CFO) calculated using DFT and magnetic properties measured via Vibrating Sample Magnetometry (VSM) used in FEA model of a magnetostrictive material.

Property	Variable	Value
Electrical conductivity	σ	178.5714~[MSm^{-1}]
Relative permittivity	ϵ	10[7]
Density	ρ	5.32 [~gcm^{-3}]
Elasticity matrix, Voigt notation	{C_{11}, C_{12},...}	{237.70, 1.5312...} [GPa] (Table S1, Supporting Information)
Saturation magnetization	M_s	228415 [~Am^{-1}]
Initial magnetic susceptibility	χ	0.7460
Saturation magnetostriction	λ_s	-18.78×10^{-4}

2.2. Magnetoelectric Effect Simulation Via FEA Modeling

Next, the FEA model was developed to study the interplay between magnetostriction and piezoelectricity in a single MENP at the nanoscale. This enabled the calculation of the generated stimulation voltage and consequently α_{MENP} (V/cm-Oe) as a function of input magnetic field. To accomplish this, all previously listed properties, either determined experimentally or via DFT calculations, were transferred to material properties of a core-shell FEA model.

The MENP's dimension was based on the average radius of CFO (25 nm) and the theoretical thickness of the BTO (7.8 nm) from the input molar ratio of 24.8% BTO and 76.2% CFO.

For the first part of the study, in accordance with the stimulation conditions to be used for the in-vivo experiments, the magnetostriction of CFO was studied to calculate its stress. A DC magnetic field (H_{DC}) at 200 mT with an AC magnetic field (H_{AC}) at 6 mT, 140 Hz was applied along the easy-axis of magnetization of CFO. We calculated an average von Mises stress of 3.4×10^7 Nm^{-2} with H_{DC} contributing 3.2×10^7 Nm^{-2} in the CFO core, as visualized in **Figure 4A**. Furthermore, the effect of varying the driving input H_{DC} on the stress output was studied while keeping the H_{AC} constant. This produced a non-linear response as

Table 2. Properties of $BaTiO_3$ (BTO) calculated using DFT and used in FEA model of piezoelectric material.

Property	Variable	Value
Density	ρ	6038.41 [kgm^{-3}]
Elasticity matrix, Voigt notation	{C_{11}, C_{12},...}	{256.37, 101.53...} [GPa] (Table S2, Supporting Information)
Piezoelectric coupling matrix, Voigt notation	e_{ij}	[0, 0, −2.7...] [C/m^2] (Table S3, Supporting Information)

© 2024 The Authors. Advanced Healthcare Materials published by Wiley-VCH GmbH

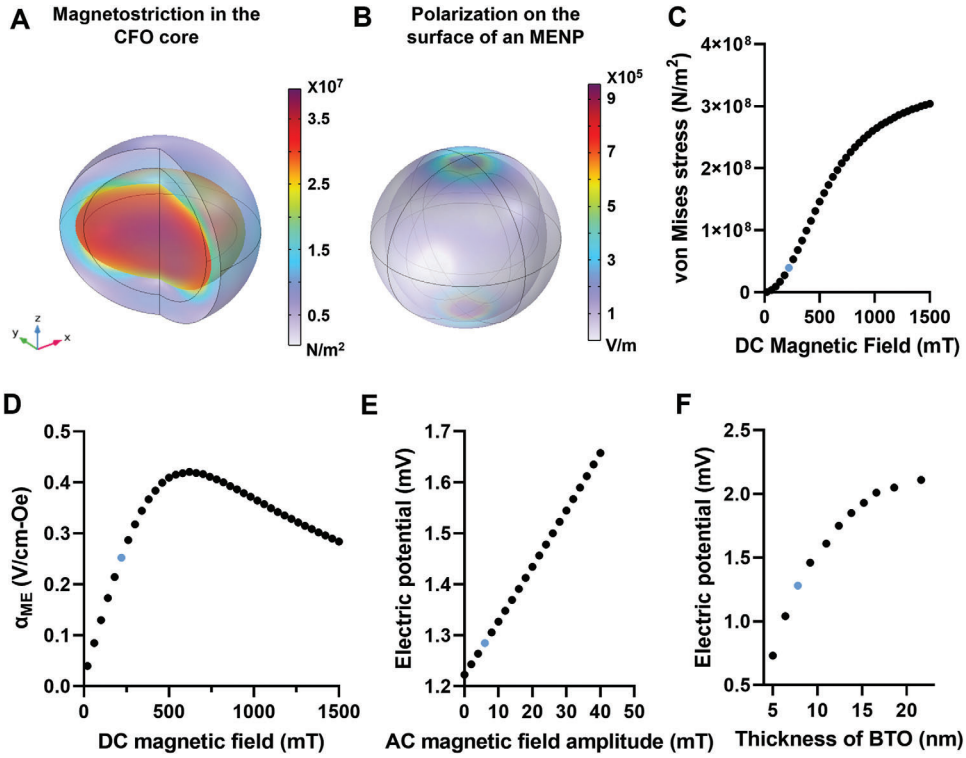

Figure 4. A) 3D rendering of the the induced stress ($Nm^{-}2$) at 220 mT DC + 6 mT, 140 Hz AC magnetic field in the magnetostrictive core of CFO. B) Figure indicating polarization (V/m) generated in the outer BTO shell on the application of the stress from A along the inner wall. C) Evolution of stress as a function of applied DC magnetic field. D) Calculated magnetoelectric coefficient (α_{MENP}) as a function of the applied field. E) Plot of linear increase in generated electric potential as AC magnetic field's amplitude is increased. F) Electric potential as a function of the piezoelectric phase i.e., thickness of the BTO shell. The blue data points in C-F represent the conditions used for further in vivo stimulation.

provided in Figure 4C. The range of stress thus obtained in this case was in the magnitude of 10^7–10^8 Nm^{-2}.

In order to understand the effects that varying stimulation parameters may have on spatial selectivity of the MENPs, a sweep was also done for the AC magnetic field amplitude from 0 up to 40 mT while keeping the H_{DC} constant at 220 mT. For studying the effect of varying thickness of the BTO layer, the outer diameter was varied to have a shell varying from 5 nm up to 23 nm for a H_{DC} of 220 mT + H_{AC} amplitude at 6 mT, 140 Hz. The von Mises stress results from these three studies (varying AC and DC magnetic field, and varying BTO thickness) were applied to the second model for piezoelectricity for studying the generated electric potential i.e., the stimulation voltage from a single magnetoelectric nanoparticle.

The maximum electric field norm (V/m) of the entire piezoelectric phase is considered for calculating the α_{MENP}, and the maximum electric polarization generated (mV) is used for further in silico brain modeling. The results have been visualized in Figure 4B. To represent the effect of varying the H_{DC}, the magnetoelectric coefficient (α_{MENP}) has been calculated (Figure 4D). It shows a typical non-linear behavior which starts to reduce after reaching a maximum value of 0.42 V/cm-Oe at 600 mT DC magnetic bias. For the operational conditions of 220 mT employed later in this work, α_{MENP} is 0.25 V/cm-Oe.

To observe the influence of the applied AC field on the resulting stimulation voltage, the potential generated due to increasing H_{AC} been presented in Figure 4E. The trend of generated electric potential for increasing thickness of the piezoelectric phase when the applied field is 220 mT DC and 6 mT, 140 Hz AC is shown in Figure 4F. A linear response is obtained for increasing H_{AC} while the electric potential for increasing BTO thickness saturates at around 2 mV for 15 nm shell.

The conducted studies facilitated the investigation into the control and prediction of stimulation voltage of a single MENP and, consequently, allow the calculation of the total stimulated area in the brain as a function of easily controllable parameters.

2.3. In silico Simulation of in vivo Experiments for Neuronal Tissue Activation

To interpret the significance of the output voltage derived from the FEA modeling, it was necessary to compute the extent of stimulation, (further called as activated area) via in silico modeling of neuronal tissue. Our FEA model of a single nanoparticle yields an electric polarization as a dipole across the particle normal to the applied field. During stimulation, the mice are able to freely move within their cage, and therefore this polarization would also move relative to the brain anatomy. For model simplicity, it is assumed that this movement was random during the stimulation time, which allowed us to treat our nanoparticle cluster as having a radially symmetric electric potential. Therefore, a range of radii of MENP bolus/cluster radius was constructed with a voltage of 1.28 mV. This corresponded to the voltage generated by a

© 2024 The Authors. Advanced Healthcare Materials published by Wiley-VCH GmbH

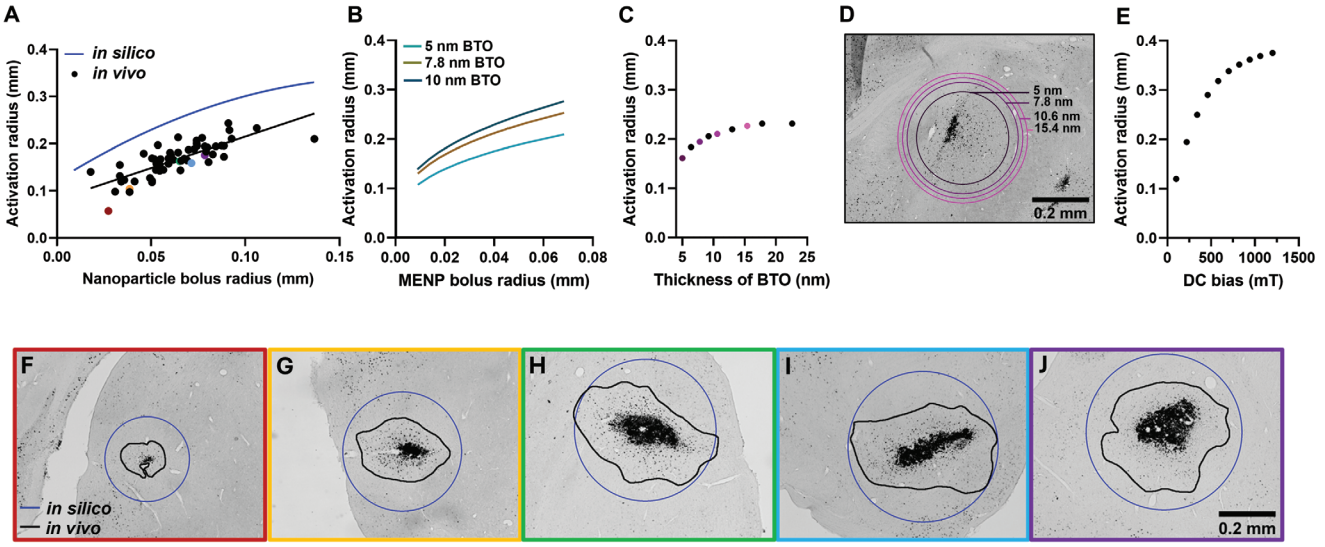

Figure 5. A) Activation radius as a function of the magnetoelectric nanoparticles (MENPs) bolus radius as determined experimentally (in vivo) and theoretically (in silico) calculated for 7.8 nm thickness of $BaTiO_3$ (BTO) shell under the stimulation condition of 220 mT DC magnetic field and 6 mT, 140 Hz AC magnetic field. B) Activation radius dependency on increasing piezoelectric phase content. C) Expected variation in the activation region as a function of increasing BTO thickness, visualized on a tissue sample (D) with the MENPs occupying an area with a radius of 0.03 mm. E) Activation radius on the application of increasing DC magnetic field while keeping the AC field constant at 6 mT, 140 Hz for a selected MENPs bolus radius of 0.03 mm. F–J) Selected c-fos tissue stainings to indicate in vivo and in silico activation radius. Color frames correspond to specific experimental activation areas as indicated in (A).

magnetoelectric nanoparticle experiencing 220 mT H_{DC} + 6 mT, 140 Hz H_{AC}. Here, the activation area has been reported as the radius of a circle extending from the centre of the MENP bolus into the tissue for a range of MENPs cluster radius from 0.01 to 0.13 mm. The activation radius then demarcates the distance into the tissue below which the spatial derivative of the generated electric field is greater than 11 kVm^{-2} extending radially from the MENP bolus surface.

The simulation yielded activation radius in the range 0.13 – 0.25 mm (**Figure** 5A,F–J). It provided a linear correlation between activation radius and the radius of the MENP. We hypothesize that the nanoparticles remain outside of the cells, based on histological analysis of nanoparticles and their interactions with phagocytotic cells,[5] however we have not experimentally confirmed this. Thus, the tissue modeling presented here relies on bulk electrical properties of grey matter, and does not explore directional analysis of nanoparticles interacting with individual neurons.

As no chemical synthesis reaction can yield nanoparticles of perfectly uniform shell thickness, it prompted further inquiry on the impact of changing BTO thickness on the generated potential and hence the activation radius for a range of MENP bolus radius. A simulation with a 5 nm-thick BTO layer was conducted, which resulted in an activation radius ranging from 0.11 to 0.21 mm (Figure 5B). Similarly a simulation run for 10 nm BTO thickness was also performed for contrast. The overall impact of BTO-layer thickness on activation radius was observed to be relatively weak. (Figure 5C).

In particular, the activation radius ranged only from 0.16 to 0.23 mm when increasing the outer layer thickness by almost five times. We observed that the BTO-shell thickness only slightly contributes to activation radius enlargement (Figure 5D). In this case, an increase of 22.5 µm was observed when the thickness grew from 5 to 6.4 nm but was as low as 4.5 µm when increasing BTO thickness from 15.4 to 17.8 nm. Activation radius quickly reached a plateau.

Instead, a stronger relationship was detected regarding the impact of DC bias on activation radius (Figure 5E). The activation radius ranged from 0.12 to 0.37 mm when increasing the DC magnitude from 100 to 1200 mT. The activation radius increased by 74.45 µm when the DC component grew from 100 to 220 mT (with steps of ≈20 µm) but only increased by 57.09 µm (with steps of ≈20 µm) when it was raised from 580 to 1200 mT. This reflects the increase observed in α_{MENP} value at lower DC fields and its drop after 600 mT (Figure 4D).

Consequently, to assess the activated area (as a function of MENP bolus) from in silico models, in vivo stimulation with the same range of MENPs bolus was conducted. For this, mice were injected with MENPs as previously described[5] and stimulated with our in vivo magnetic coil. Briefly, 30 naïve mice (C57Bl/6J) were injected bilaterally in the subthalamic region with dosages ranging from 5 to 100 µg. The highest concentration of 100 µg was chosen based on previous toxicity analysis.[5] Mice were then stimulated with a magnetic fields and post-mortem brain sections were immunohistochemically stained against c-fos protein, which is widely used as a marker of neuronal activity.[26]

Magnetoelectric stimulation by MENPs significantly increased the number of c-fos positive cells in the area surrounding the injection site (Figure S2). This corresponds well with previous findings in which the authors also observed an increase in c-fos activity following magnetic stimulation of MENPs, as compared to negative controls, (i.e., MENPs without magnetic stimulation, magnetostrictive-only nanoparticles with magnetic stimulation).[5] Furthermore,no heat is expected to be generated

© 2024 The Authors. Advanced Healthcare Materials published by Wiley-VCH GmbH

from the MENP as the heat generated is directly proportional to the integral of the BH curve loop. As no hysteresis is measurable (Figure 1H in ref. [5]) when applying the AC magnetic field used both experimentally, and in the simulation in the current manuscript, the hysteresis loop integral, and hence the heat output, is zero.

It was found that the radius of tissue with c-fos positive cells surrounding the MENP injection site (activation radius) was dependent on the MENP bolus (Figure 5F–J). Quantification of the area of the MENP bolus versus the activation area revealed a correlation between them (r = 0.7827) (Figure 5A).

The observed median percentage error between simulated and experimental results for 7.8 nm BTO thickness was 31.04%, reflecting that results obtained in silico and in vivo remain within the same order of magnitude and provided further confirmation for a linear correlation between MENPs bolus radius and activation area. Results with 5 nm BTO thickness MENPs are closer to the in vivo experimental activation radii as the median percentage error fell to 26.65%.

3. Discussion

The primary objective of this work is to provide a comprehensive investigation of MENPs as untethered nanoelectrodes for spatially selective neuronal stimulation. This involves the synthesis of MENPs, development of a multi-scale model accompanied by analysis, and corroboration with in vivo stimulation experiments.

The modeling process built on Finite Element Analysis (FEA) takes into account diverse influences on the magnetoelectric effect by utilizing atomistic properties calculated by DFT, as well as experimental nanoscale properties of synthesized MENPs. It is therefore capable of predicting the area of stimulation for a given amount of MENPs with known material properties. This methodology provides for a streamlined and thorough approach in assessing the effectiveness and feasibility of MENPs in achieving spatially selective stimulation of neural tissue.

A sol–gel method for BTO growth on CFO was selected due to advantages such as low reaction temperature, high yield, and relatively high purity. The reactions involved are hydrolysis of the precursors and condensation to obtain a continuous 3D network enhancing the coupling between BTO and CFO. Experimental confirmation of their morphology and composition, via VSM, XRD, and TEM allowed us to confirm their suitability for in vivo stimulation.

Our FEA analysis method has been designed to work with the minimum number of properties to facilitate an easily accessible simulation method, and without the need for sophisticated experiments. Thus the critical parameters can be distilled down to the following: a) magnetic properties of CFO, which includes its saturation magnetization M_s, initial magnetic susceptibility χ and saturation magnetostriction λ_s, b) piezoelectric properties of BTO, which includes piezoelectric coupling constant (e_{ij}) and spontaneous polarization P_s, c) common properties of the two phases, which entails their density (ρ) and their elastic constants (C_{ij}).

For determination of these properties, either theoretical calculation or experimental data has been used based on ease of access and simplicity. For example, ferrimagnetic materials composed of transition metal oxides with perovskite structure are still an active area of research in the field of computational materials science. Therefore, CFO, which although exhibits high magnetostricion and is a good choice for MENPs, is complicated to probe due to limitations in existing quantum mechanical magnetic models.[27,28] However, in the form of polycrystalline nanoparticles, measuring the CFO magnetic hysteresis curve is much more feasible and relies on commonly available university equipment. This also eliminates the problem of scrutinizing details such as pinning loss or domain wall movements, which are difficult to control or directly modulate via synthesis parameters. Conversely, there exists open-source, automated workflows for determining elastic and dielectric properties of materials without excessive computational demands.

Concerning the magnetic experimental data, a squareness ratio of 0.56 indicates uniaxial anisotropy with presence of non-interacting single domains.[15] Therefore, in the FEA model, the magnetization has been applied along the easy-axis of the MENPs. In our work, we directly probed the magnetostriction of CFO nanoparticles with XRD bypassing reliance on literature values typically available for pure, single crystals. This allows us to obtain the overall λ_S for our polycrystalline sample that can be related to λ_{100} and λ_{111} with the following relationship:[29]

$$\lambda_S = \frac{2\lambda_{100} + 3\lambda_{111}}{5} \tag{2}$$

In relation to piezoelectric properties of BTO, most experimental designs involve the fabrication of pellets, which often requires milling, sintering and poling, all of which can affect the nanostructure and lead to formation of impurities, reduced contact, and pores.[30] Therefore, with theoretical investigation, the value for P_s is higher than experimental values but matches well with other theoretical calculations from first principle.[31] The values for e fall well within reported experimental range of 150–300 pC/N (dependent on the method of synthesis, sintering temperature etc.) and matches well with other theoretical works.[32,33]

Based on these considerations, the α_{MENP} value and dependency of the generated electric potential from a single MENP has been conducted. The α_{ME} in single phase multiferroics requires a nine component magnetoelectric susceptibility tensor.[34] However, for a two-phase composite, we can define magnetoelectric coefficient (α_{MENP}) as $\frac{\partial E}{\partial H}$ in pseudo-linear regime and under closed circuit conditions, can be integrated as:

$$\alpha_{MENP} = \left(\frac{\partial E}{\partial H}\right) = \frac{1}{t}.\left[\frac{\partial V}{\partial H}\right] \tag{3}$$

This approximation works specially well when the MENPs work on non-resonant frequency and low magnetic field inputs.[35]

While some prior studies have explored Finite Element Analysis (FEA) models, they rely on utilizing bulk material properties or material databases, which can lead to substantial inaccuracies. For example, reported value of saturation magnetization vary by orders of magnitudes from kA/m to hundreds of kA/m in the literature.[4,36] Achieving an exact match between properties of synthesized nanoelectrodes and bulk material remains an impractical endeavor due to inherent differences in scale. This limitation becomes especially pertinent when considering the expansion toward spatial selectivity and multiplexing. One of the predominant strategies currently employed to tailor the behavior

© 2024 The Authors. Advanced Healthcare Materials published by Wiley-VCH GmbH

of MENPs is to tune material properties, as well as morphology at the nanoscale. For instance, in the case of CFO, varying the degree of incorporation of Co and Fe atoms into the spinel lattice dictates the degree of inversion and is responsible for change in its properties. This precise gap can be overcome by employing DFT-driven calculation for material properties.[16,21,37] As such, our work employs a model for FEA analysis of MENPs, which closely mirrors the synthesized counterparts, while ensuring a manageable level of complexity.

In addition, with comparison with in vivo stimulation data, we move beyond a qualitative to a quantitative assessment. The in vivo results show that both the scope of stimulation and the number of neurons stimulated can be controlled by the volume of MENPs injected (Figure S2, Supporting Information). Further research regarding MENPs' volume and corresponding neuronal activation will thus be able to show, how to reduce undesirable side effects while ensuring the efficacy of stimulation.

The phenomenon of excitation of neurons with extracellular voltage can be understood through the activation function (f).[38] However due to lack of knowledge of the geometry, orientation, and morphology of the neurons, it is not possible to calculate the activation function as it is a function of the transmembrane potential along the neuron fibers. Therefore, for determination of neuronal activation threshold, the literature often provides two parameters to determine the minimum electrical stimulation required to elicit an action potential. These are the primary electric field $\vec{E}$ and the spatial derivative of the primary electric field $\nabla_r \vec{E}$, also known as which is directly proportional to the neuronal activation function [39]. Activation thresholds reported for $\vec{E}$ differ across the literature [39–42], but are the least sensitive to axon length [40], while thresholds reported for these electric fields using $\nabla_r \vec{E}$ remain within the same order of magnitude[40,41] even when the mode of stimulation is different.

Moreover, the primary electric field to determine the activation threshold have been more commonly used for computational models that rely on time-dependent, current injection directly into the tissue for stimulation where the threshold transmembrane voltage is a function of the pulsewidth.[43] However, this can lead to an underestimation of the spatial extent of the local neural activation, especially for areas around the curvatures of the electrode[44,45] and also where the neuron bends or branches.[46] Therefore, other methods such as TMS (Transcranial Magnetic Stimulation), which uses an AC magnetic field to induce stimulation also use the gradient of the electric field to determine the volume of activated tissue.[47] Electric field gradient has also been applied for modeling activated volume in the case of Deep Brain Stimulation (DBS), which uses electrodes for stimulation, without the explicit computation of axon models.[48] In both cases the tissue activated is in the order of milimeters or greater and therefore accounting for individual neurons would be tedious.

Although less frequently explored in conventional tissue models, $\nabla_r \vec{E}$ works better as the activation threshold parameter for arbitrary shaped electrodes with extracellular stimulation with bulk, inhomogeneous properties of the surrounding tissue[44,49] and is sufficient to predict excitation.[50] Studies with implanted micro-coils have also utilized the spatial gradient of the electric field to investigate suprathreshold fields for indirect stimulation. The effectiveness of the stimulation is largely influenced by the design of the microcoils, particularly their shape.[51] Notably, a threshold value of 11 kVm^{-2} has been adopted as a conservative estimate in these studies[52] although higher threshold values have also been used in the literature.[53] Therefore, due to the similarities between the stimulation strategies such as in TMS and implanted micro-coils and this work, the value of 11 kVm^{-2} derived from TMS thresholds[41] has been used to account for electric potential changes across two spatial dimensions as the minimum threshold for activation when stimulated with an extracellular voltage, reflecting more accurate neuron models for a quasi-static approximation.

To enable easier comparison with other works, the induced electric field at the activation threshold of 11 kVm^{-2} can also be considered. In the case of microcoils (as they exhibit the same degree of spatial selectivity as our nanoparticles), and monopolar point electrodes (which also relies on electric field gradient for defining activation threshold), the electric field reported at the activation threshold is in the same order of magnitude of ≈1–10 Vm^{-1} at low frequencies.[41,51] Electric fields in the range of a few V/m are also known to be capable of evoking neural spikes.[54] In this work, the electric field is also in the same order of magnitude (e.g., approximately at the center of Figure 5A, the stimulation threshold at 11 kVm^{-2} corresponds to a 1.4 Vm^{-1} E-field which would at a distance of 0.2 mm create a potential of 0.28 mV). The exact value of the electric field for Figure 5F-J has been reported in the supplementary Table S4 (Supporting Information). In the works cited here, the extent of activation is around 2 to 3 times the cross-sectional width of the electrode/microcoil, and which also holds true for the MENP bolus (Figure 5A), further substantiating the validity of the assumptions made and the adopted modeling parameters.

Notably, there is an agreement between experimental data and simulation results, revealing direct correlation between activation distance and injected MENPs' bolus radius as seen in Figure 5A,F–J. This linearity is most prominent when closer to the median of the tested MENPs bolus' radii range. Given this feature, a fixed radius that lies near the center was used to test additional controllable parameters, DC magnetic field and shell thickness, on the activation radius.

Our simulation studies show that for a given radius of injected MENPs, the activation area is less easily modulated by the specific thickness of the outer shell and more by the volume of the MENPs as seen between Figure 5B,C. Figure 5D allows for easy visualization of this effect on activation area on changing the thickness of BTO while keeping the radius of injected MENPs constant. This shows that the contact area between the magnetostrictive and piezoelectric phases plays a much critical role than the overall dimension of the MENPs. Besides, on the basis of Figure 5C, one can propose that if the thickness of the piezoelectric phase is known, or if it varies by some nanometers, the activation radius can still be predicted and controlled on the basis of MENPs dose.

Additionally, simulation results provide evidence of spatial selectivity when employing MENPs. By increasing the DC magnetic field at which the MENPs operate, the activation radius can grow higher than 20 µm as seen in Figure 5E. While working with high magnetic fields may be impractical, the observations show that the most considerable differences in activation radius are achieved when the magnetic fields lie within 100 and 600 mT

© 2024 The Authors. Advanced Healthcare Materials published by Wiley-VCH GmbH

with 6mT, 140 Hz AC field for MENPs evaluated in this work. Therefore, modifications in input parameters based on the trend of the α_{MENP} can yield an increased activation area within neural tissue in the order of tens of μm value. However, the exact value would depend on the chemical composition of the MENPs employed.

To the best of the authors' knowledge, this work is the first to report on spatial selectivity using MENPs as wireless nanostimulators. It establishes MENPs fine-tuning versatility as a key benefit compared to other neurostimulation methods. Despite the promising results, further experimental validation is still required.

For example, because the surface voltage is equivalently distributed, an MENP bolus whose radius tends to infinity will result in an electric field of virtually zero magnitude. This becomes relevant when considering the small intrinsic surface potential of individual MENPs, as agglomeration into clusters could result in comparably lower surface area.

To summarize, our observations suggest that the activation radius is governed by the total area occupied by the nanoelectrodes/MENPs, serving as an explanation for the non-linear behavior detected when the MENP bolus radius is too small or too large. As such, achieving a balance between MENP properties and cluster size is imperative for predictable neurostimulation.

We acknowledge that the model may only partially depict the underlying stimulation mechanisms but is nonetheless a fundamental step toward understanding spatial selectivity for neural stimulation. We propose that accounting for properties of adjacent brain tissues can be omitted given the bolus size and placement mechanism, in order to reduce model complexity. Unlike transcranial stimulation, the external field necessary to elicit magnetoelectricity reaches its target with negligible variation when an adequate Helmholtz coil configuration is employed. However, implementing altered tissue properties due to glial scarring and fibrous encapsulation[39] would enrich the model.

Altogether, the experimental results concerning the dependence of the MENP bolus radius and the activation area confirm the data we obtain from the simulation. In all cases, the simulated results predicted a larger activation area than what was observed experimentally. This is due to some degree of overoptimization within our models such as the assumption that an injected bolus has a packing density of 100% MENPs. It is of course possible to make estimations to reduce this. For example, estimating the MENP bolus to be of 70% yield rather than 100% would reduce the activation radius. However, we have limited these to the latter value to maintain the overall simplicity of our model. Furthermore, the model is based on core-shell MENPs, although the synthesized nanoparticles are not strictly of uniform core-shell structure, a discrepancy that can also be addressed in future models. Furthermore, the model can be improved by raising the accuracy of the computed material parameters through better selection of pseudopotentials and expanding it to include frequency dependent properties.

4. Conclusion

In this work, a model was developed and tested as part of primary undertaking to quantify the extent of tissue activation as well as discuss the impact of stimulation parameters of MENPs on spatially selective activation. Overall, we successfully synthesized MENPs, along with experimental and computational determination of material parameters for the magnetostrictive CFO core and piezoelectric BTO shell. This information was used to inform a FEA model that subsequently provided the stimulation voltage of a single magnetoelectric nanoparticle. Although the exact mechanism of activation of neurons with MENPs is not well understood, by utilizing in silico models, we simulated the activation radius corresponding to the administered MENPs dosage, achieving good agreement with in vivo results at an activation threshold of 11 kVm^{-2}. Furthermore, the magnitude of the driving magnetic field (for a given bolus size) had a strong effect. Therefore, relative to other controllable parameters such as piezoelectric shell thickness and AC magnetic field, the DC magnetic field is certainly facile to external modulation of spatially selective of neurostimulation. A comparison of our simulated results to experimental data validated our model. Hence, the precise control of the area to be stimulated is possible with wireless nanostimulators working on magnetoelectricity and its magnitude can be evaluated with the methodology given here.

In summary, the method outlined in this paper, combining materials modeling, and physics simulation, offers a practical and widely applicable approach for predicting spatial stimulation in neural tissues with magnetoelectric nanostimulators. We expect this method to serve as a fundamental tool for evaluating emerging neural stimulation technologies, facilitating the advancement of nanoscale devices.

5. Experimental Section

Experimental Synthesis and Material Characterization—Magnetic Characterization of CFO: $CoFe_2O_4$ (CFO) nanoparticles (radius 25 nm) were purchased from Sigma–Aldrich to serve as the core of the core-shell MENPs. The magnetic hysteresis was recorded with a MicroMag magnetometer (Vibrating Sample Magnetometer). The sample (1.415 mg) was sealed into a quartz tube and affixed to the probe, demagnetized and exposed to magnetic field with the range ± 3.18 kAm^{-1} at room temperature (Figure 2A).

Experimental Synthesis and Material Characterization—Magnetostriction Characterization of CFO Nanaoparticles: Approximately Sigma–Aldrich CFO nanoparticle (2 g) was mixed with ethanol to prepare a suspension mixture deposited on a Si(111) wafer to create a homogeneous and thin layer on the wafer post-ethanol evaporation. A standard Bruker D8 XRD sample holder was modified to accommodate a magnet under the Si wafer. Change in lattice parameter of CFO was measured for different magnet strengths (Figure 2B). Data analysis was performed with Diffrac.Topas by Bruker. During data analysis, it was confirmed that the change in lattice parameter was at least one order higher than the device error.

Experimental Synthesis and Material Characterization—Synthesis of MENPs via Sol–Gel: Following a typical sol–gel process,[55] first CFO nanoparticles (Sigma –Aldrich, 30 nm; 10 $mgml^{-1}$) were dispersed in deionised water and heated to 80°C. Concurrently, oleic acid was introduced to the mixture at a weight percentage of 30% relative to CFO. The temperature was elevated to 90°C and maintained for 30 min, after which the temperature was reduced by 30°C to add octane in a 1:1 volume ratio. The obtained organic phase yielded ferrofluid immiscible with the aqueous phase.

Barium acetate and titanium butoxide were used as precursors for synthesizing barium titanate. These were dissolved in glacial acetic acid with stearic acid to promote the coupling of CFO and BTO nanoparticles. The ferrofluid was then added to the BTO solution. To this solution at a ratio of metal ions and citric acid of 4:1. The final nanoparticles were centrifuged

© 2024 The Authors. Advanced Healthcare Materials published by Wiley-VCH GmbH

at 7000 rpm for five minutes and washed thrice. The nanoparticles were dried overnight at 90°C and then calcined at 800°C for 1 h.

Experimental Synthesis and Material Characterization—Energy Dispersive X-Ray Spectroscopy of MENPs Morphology and Elemental Mapping: High-Angular Annular Dark Field Scanning Transmission Electron Microscopy (HAADF-STEM) combined with Energy Dispersive X-ray Spectroscopy (EDXS) was used to investigate the chemical composition of $FeCoO_x$ – $BaTiO_y$ nanoparticles (Figure 2C; Figure S1, Supporting Information) using FEI Tecnai Osiris ChemiSTEM microscope at 200 keV energy and a Super-X EDXS system. EDXS spectra was quantified with the FEI software package TEM Imaging and Analysis (TIA) v4.7-SP3. Using TIA, element concentrations were calculated based on a refined Kramers' law model, which included corrections for detector absorption and background subtraction. For this purpose, standard-less quantification, i.e., through theoretical sensitivity factors without thickness correction, was applied.

Experimental Synthesis and Material Characterization—X-Ray Diffraction Analysis of MENP Crystal Structure: The composition of the synthesized MENPs were confirmed using a Bruker D8 XRD. MENPs were placed on a Si (111) wafer, and the corresponding spectrum in Figure 2D was obtained with Cu radiation operating at 40 kV/40 mA. Diffraction peaks were captured from 10°–45° with increments of 0.015°. The obtained diffractogram was matched with that of CFO and BTO as per the Crystallographic Open Database (COD). Background correction was done via OriginPro 2022.

Quantum Mechanical Calculations of Intrinsic Properties of BTO and CFO—Mechanical Properties of BTO: The tetragonal unit cell of barium titanate from COD 1507756, with the cell parameters as $a = b = 3.9915$ Å, $c = 4.025$ Å (Figure 2B) was first structurally optimized using open source code Quantum Espresso.[56,57] For this calculation, the kinetic energy cut-off was set as 40 Ry for plane wave basis and charge-density as 400 Ry for GBRV ultra-soft pseudopotential (USPP).[58] The k-point grid was determined to be $8 \times 8 \times 8$ using the Monkhorst-Pack, while the ordinary Gaussian smearing term was calculated as 0.004 Ry. In order to prevent the transition of the tetragonal unit cell to an orthorhombic state, the *c/a* ratio was constrained, and the volume of the cell was kept constant for unit cell optimization.

The bulk modulus of the crystal was calculated with Murnaghan EOS. Elastic tensor (6×6) for BTO were determined using *thermo_pw.x* extension for Quantum Espresso and are reported in Table 1.[59] These were calculated by a small displacement relative to the original co-ordinates by changing the value of c in steps of 0.5 starting from 7.328 alat up to 7.6928 alat while keeping *c/a* ratio constant and performing SCF by relaxing the ions between each distorted lattice parameter.

Quantum Mechanical Calculations of Intrinsic Properties of BTO and CFO—Piezoelectric Properties of BTO: The value of spontaneous polarization was computed through Berry phase calculations as a function of strain (stress). Its slope provided the piezoelectric coefficient and could be scaled for a "finite" interpretation.[60,61] The Ti atom was moved from its equilibrium position by ±0.001 of its fractional coordinates along the c-axis. This imitated the application of stress (σ_{33}) on one side/surface of the unit cell. While keeping the lattice constant ($a = b$, c/a) of the unit cell unchanged, the position of the titanium atom and barium atom was allowed to relax along the strained axis, keeping all angles fixed. The new positions of Ba and Ti, as well as the new *c* were obtained from the last SCF run.

Quantum Mechanical Calculations of Intrinsic Properties of BTO and CFO—Mechanical Properties of CFO: For electronic structure calculation and structure optimization, fractional coordinates were adopted from a unit cell of $CoFe_2O_4$ (CFO) from Materials Project 753222, which was used to perform the structural optimization with Quantum Espresso v7.0 and earlier. The lattice parameters were fixed using $a = b = c = 8.3697$ Å. The k-point grid was set at $8 \times 8 \times 8$. The parameters used for this calculation were determined as kinetic energy cut-off 40 Ry and charge density cut-off 400 Ry with degauss value as 0.01 and cold smearing with PBEsol (PBE functional for solids) pseudopotentials for projector augmented wave method (PAW) generated with scalar relativistic corrections.[62] The energy conversion and interatomic force were set as less than 1.0×10^{-4} Ry. The mechanical properties were determined for the optimized cell containing 14 atoms to reduce the computational demands and are reported in Table 1. XcrySDen and VESTA were used for adjusting unit cell length and visualization.

Finite Element Analysis (FEA) of Magnetoelectric Output of a MENP: For modeling the MENPs nanoparticles using FEA, COMSOL Multiphysics 6.1 was used. The modeling was done divided into two domains where the stress response from DC and AC field was calculated and consequently transferred to a second model for the piezoelectric response.

In the 2D axis-symmetric study, the nanoparticle was modeled anisotropically as a core of 25nm CFO (Figure 4A). The outer shell was set to 7.8 nm thick BTO shell. The average BTO thickness was calculated using the stoichiometric ratio of BTO:CFO. The properties obtained via DFT calculations and experiments for CFO and BTO are given in Table 1 and 2. For CFO Effective B-H curve was used with a Langevin function to approximate the magnetic behavior. The Magnetic Fields and Solid Mechanics modules were used for Magnetostriction multiphysics coupling.

Using the in-built Multiphysics study module of COMSOL, a range of DC and AC magnetic fields were applied ($\vec{H}$). Both types of magnetic fields were applied in-plane as a uniform magnetic flux and solved for a reduced field, i.e., the source of the magnetic field was omitted, and the generated magnetic field was a known variable (inset in Figure 4A). The study, in frequency mode, uses Ampere's Law:

$$\vec{B} = \nabla \times (A_b + A_r) \tag{4}$$

$$\vec{B} = \mu_o[\vec{H} + \vec{M}(\vec{H}, S_{mech}) + \vec{M}_r] \tag{5}$$

The software solved for the magnetic vector potential $\vec{A}$ (background and reduced) whose curl is the vector field $\vec{B}$, which is then consequently used to obtain the $\vec{H}$ as a function of $\vec{B}$. μ_o is the magnetic permeability, $\vec{M}$ is the magnetization and S_{mech} is the stress tensor for a linear elastic material. The outer boundary was kept fixed to prevent movement of the nanoparticle as a whole i.e., the fixed outer boundary was provided to allow for smooth convergence of the solution by imposing a boundary condition on the global degrees of freedom. A boundary condition of the magnetic insulated core was applied to prevent any deviation of the magnetic field through CFO such that the normal components of applied magnetic flux density were zero ($\vec{n} \cdot \vec{B} = 0$).

For the piezoelectric output, a second 3D model with only the outer shell and identical boundary conditions was constructed as shown in Figure 5B using the Electrostatics and Solid Mechanics for the Piezoelectric of COMSOL to solve for the following equations:

$$\nabla \cdot \vec{D} = \rho_V \tag{6}$$

$$\vec{n} \times \vec{E} = 0; \quad \vec{n} \text{ is the surface normal} \tag{7}$$

$$\int_{\partial\Omega} (\vec{D} \cdot \vec{n}) dS = Q_0 \tag{8}$$

where $\vec{D}$ is the electric displacement field (SI unit $Cm^{-}2$), ρ_V is the electric charge concentration (SI unit Cm^{-2}). Ω is the surface boundary and Q_0 is specific charge (SI unit *C*). COMSOL then solves for the electric field from electric potential V as $\vec{E} = -\nabla V$. Further details on the equations can be found in the AC/DC User Manual of the software.

Additionally, the inner walls of the domain were selected as electrical grounding to ensure close circuit conditions following the standard piezoelectricity measurement method. This implies that there was zero potential across the inner boundary (V = 0); the inner core was an insulator. The outer wall was considered to had a floating potential. The stress generated from the magnetostrictive model was applied as pressure to the inner wall of the BTO shell. The α_{MENP} was calculated by dividing the generated voltage field norm (Vcm^{-1}) by 220 mT DC magnetic field (Figure 4D). The maximum potential generated was recorded for a sweep of DC magnetic field, AC magnetic field, and BTO thickness by a domain probe and was used for further calculations of activation area in brain tissue models (Figure 4E and F).

© 2024 The Authors. Advanced Healthcare Materials published by Wiley-VCH GmbH

In-vivo Magnetic Stimulation in Freely Moving Mice—Animals: Experiments were performed on 30 male naïve mice (C57Bl/6J; Jackson Laboratory). Animals were socially housed in a reversed 12-h day-night rhythm under controlled temperature and humidity with ad libitum access to food. All animal experiments were performed under Directive 2010/63/EU for animal experiments under the permission of the Maastricht Institutional Animal Welfare Committee of Maastricht University, Maastricht, The Netherlandsand the National Institute of Health Guide for the Care and Use of laboratory animals. The protocol was approved by the by the Maastricht University Animal Ethics Committee (project license number AVD1070020186046).

In-vivo Magnetic Stimulation in Freely Moving Mice—MENP Injection: 30 min before the start of surgery, an analgesic (buprenorphine, 0.1 $mgkg^{-1}$) was injected subcutaneously. Anesthesia was induced by inhalation of 4% isoflurane (Abbot Laboratories, Maidenhead, UK) and maintained at a concentration between 1.5–3%. Animals were restrained under anesthesia in a stereotactic small animal frame and placed on a thermoregulation pad to maintain body temperature at 37°C during surgery. An eye lubricant was applied to counteract the drying of the eyes. At the incision site, 1% lidocaine (Streuli Pharma, Uznach, Switzerland) was injected subcutaneously as a local anesthetic. Drill holes were made above the subthalamic area (AP 2.06 mm ±1.50 mm, DV 4.50 mm). A total of 2 µl MENPs with different dosages ranging from 5 µg up to 100 µg to get different MENPs bolus volumes were injected at an infusion rate of 100 $nlmin^{-1}$ (Nanoject II, Drummond Scientific). The highest dosage of 100 µg was chosen based on the previous study where no toxicity was observed.[5]

In-vivo Magnetic Stimulation in Freely Moving Mice—In-vivo Magnetic Stimulation: Magnetic stimulation was performed by applying a 220 mT DC field paired with a 6 mT, 140 Hz AC field via a custom coil system where the mice could move freely, as previously described.[5] The magnetic field was produced with Helmholtz coils of 70 mm separated by 80 mm. With 400 turns, 2.25 A of current was required to produce the AC field with a lock-in amplifier, and commercially available permanent magnetis were used for the DC field. Mice were stimulated for 180 s with the coil switched on. The magnetic field strengths were monitored using a magnetometer.

In-vivo Magnetic Stimulation in Freely Moving Mice—Animal Sacrifice: After mice were deeply anesthetized with pentobarbital, transcardiac perfusion with Tyrode buffer was performed, followed by fixation with ice-cold 4% paraformaldehyde in 0.1 M phosphate buffer. After removal from the skulls, the brains were fixed overnight in 4% paraformaldehyde. They were then placed in 20% sucrose at 4°C for 24 h to protect them from cold damage. Coronal brain sections (20 µm) were then cut using a cryostat before being stored at −80°C.

In-vivo Magnetic Stimulation in Freely Moving Mice—c-Fos Immunohistochemistry: For c-fos staining, tissue sections were incubated for two nights with a primary antibody against the c-fos protein (polyclonal rabbit; 1:1000; Abcam, ab190289). Sections were then treated with a secondary antibody (donkey anti-Rabbit; 1:400; Jackson ImmunoResearch Laboratories Inc) and an avidin-biotin-peroxidase complex (1:800; Elite ABC-kit, Vector Laboratories). Staining was visualized with 3,3'-diaminobenzidine (DAB).

In-vivo Magnetic Stimulation in Freely Moving Mice—Quantification of MENP Distribution at the Injection Site: Stained sections of the thalamus were imaged from three rostrocaudal anatomical planes starting at the bregma (AP: -0.58, -0.94, and -1.22), with a 10× magnification. An Olympus AX 70 microscope (Olympus, Zoeterwoude, The Netherlands) with an Olympus DP70 digital camera and Cell P software (Olympus Soft Imaging Solutions, Münster, Germany) was used. Using ImageJ software [version 1.52; National Institutes of Health (NIH), Bethesda, USA], the respective areas (mm^2) of nanoparticles and surrounding tissue with a significantly increased amount of c-fos positive cells (activation area) were measured. The nanoparticle area was defined as the region of the nanoparticle injection volume within the tissue. The activation area was defined as the area around the nanoparticle injection site with the highest intensity staining of c-fos-positive cells. A cell was classified as c-fos positive when the staining intensity surpassed the background level significantly. A mean value per mouse was calculated from the respective individual areas of the three rostrocaudal anatomical sections. The corresponding mean value of the areas were then converted into an average radius (mm) of a circular activation area to compare the results with those of the simulation. A manual evaluation with blinded assessment was performed, and an average of three sections per subject was used for statistical analysis.

In-vivo Magnetic Stimulation in Freely Moving Mice—Statistical Analysis: Statistical analysis was performed using GraphPad Prism 9.4.0 (GraphPad Software, San Diego, California, USA), and immunohistochemical data were analyzed using a correlation plot between c-fos positive cells within the activation radius and nanoparticle area.

In-silico Modeling of Stimulation Area using MENP Clusters—Electromagnetic Model of MENP Cluster: An MENP bolus was defined as the aggregation of individual particles, assuming these adopt a homogeneous distribution within a spherical-shaped cluster around the point of injection int the thalamus. The area occupied by this sphere was significantly greater than that of a single particle. Hence, the latter behaves as a point charge with respect to the cluster. The voltage of individual particles (V_{NP}, obtained in Section Finite Element Analysis (FEA) of Magnetoelectric Output of a MENP) was then used to estimate the cluster surface voltage V_S using Coulomb's law:

$$\vec{E} = \frac{k \cdot q}{r^2} \tag{9}$$

$$|V_{NP} - V_S| = \left| - \int_{r_{NP}}^{r_S} \vec{E} \cdot dr \right| \tag{10}$$

$$V_{NP} - V_S = -\frac{q}{4\pi\epsilon_0}\left[\frac{1}{r_S - r_{NP}}\right] \tag{11}$$

$$V_{NP} = V_S \xrightarrow{when} r_S >> r_{NP} \tag{12}$$

where $\vec{E}$ is the electric field, k is Coulomb's constant, q is the nanoparticle charge, r is the distance from charge q in any spatial dimension, r_{NP} and r_S represent the nanoparticle and cluster radius, respectively, and ϵ_0 is the permittivity of free space. In experimental conditions, the mice were able to freely move within their cage, and thus the orientation of the brain (and consequently of the nanoparticles) to the applied field changed throughout stimulation with animal movement. The model was designed using the assumption that this orientation was random within the stimulation time. Thus, the electric polarization on the surface of the nanoparticle cluster was modeled as a uniform surface potential, making the tissue model radially symmetric. Finally, this model was built using the electromagnetic low-frequency Ohmic Quasi-Static solver in SIM4LIFE software v7.2 (ZMT Zurich MedTech AG, Switzerland).

In-silico Modeling of Stimulation Area using MENP Clusters—Stimulated Area as a Function of Injected Volume: Based on the experimental data slices, the area occupied by MENPs in tissue determined the radii used to model the spherical clusters. A single sphere was embedded in two gray matter solids to improve grid discretization (> 10 MCells). The simulation was set up at 140 Hz, and tissue properties were automatically adjusted (Table S5, Supporting Information). The MENP cluster V_S was fixed at 1.28 mV (6 mT at 140 Hz AC + 220 mT DC bias, 7.8 nm-thick outer layer), acting as the Dirichlet boundary condition of the model. Next, the electric field in any 2D plane was visualized in SIM4LIFE. This data was exported for further analysis.

In-silico Modeling of Stimulation Area using MENP Clusters—Stimulated Area as a Function of Other Adjustable Properties: The DC component of the magnetic field and the thickness of the BTO shell, were identified as elements that tune the stimulation area. Models testing the correlation between activation radius and each of these properties were also built. The framework described in Section In-silico Modeling of Stimulation Area using MENP Clusters—Stimulated Area as a Function of Injected Volume was used for these models. Instead of using a fixed boundary condition with varying radii, a single MENP cluster radius (0.03 mm) was set. Hence, the V_S changed as a function of DC bias or BTO-layer thickness. For the first, the DC field ranged from 100 to 1200 mT. For the latter, the BTO thickness ranged from 5 to 22.6 nm. The data was exported for further analysis.

© 2024 The Authors. Advanced Healthcare Materials published by Wiley-VCH GmbH

In-silico Modeling of Stimulation Area using MENP Clusters—Estimation of Activation Radius: Custom scripts in MATLAB v9.13 R2022b were developed to compute the activation radius. For each sphere, a cubic spline fit was used to approximate $\vec{E}$ from SIM4LIFE 2D-plane data. Next, this function was differentiated with respect to distance ($\nabla_r \vec{E}$). This spatial gradient was compared against 11 kVm^{-2}, an activation threshold reported for TMS and microcoils.[41] The intersection between $\nabla_r \vec{E}$ and 11 kVm^{-2} determined the distance at which neuronal firing ceases. These were reported as activation radii and compared with the experimental results (Figure 5A). Finally, the percentage error between each observation and simulation result was computed.

Supporting Information

Supporting Information is available from the Wiley Online Library or from the author.

Acknowledgements

H.W., A.M., and J.E.L. contributed equally to this work. The authors would like to acknowledged the Department of Biosystems headed by Prof. M. Franzreb at the Institute of Functional Interfaces (Karlsruhe Institute of Technology). In particular, the authors thank Dr. P. Weidler and Avishek Sarbajna for the assistance of XRD measurements of the nanoparticles, as well as Muhammad Hashsham Chishti for assembling the magnetic coils. The authors also thank Abdelhamid Benazzouz for his help with animal experiments. The authors would like to thank the Laboratory for Electron Microscopy (LEM, Karlsruhe Institute of Technology) for carrying out TEM and EDXS and for completing elemental analysis of the nanoparticles. The authors also thank the Leibniz Supercomputing Centre (LRZ) for providing with the computational infrastructure. The authors would like to thank the Michael J. Fox Foundation, the Munich Institute of Robotics and Machine Intelligence, and the Elite Network of Bavaria for funding.

Open access funding enabled and organized by Projekt DEAL.

Conflict of Interest

The authors declare no conflict of interest.

Data Availability Statement

The data that support the findings of this study are available from the corresponding author upon reasonable request.

Keywords

brain stimulation, finite element analysis, magnetoelectric materials, wireless bioelectronics

Received: August 28, 2023
Revised: January 17, 2024
Published online: February 13, 2024

[1] D. Dominguez-Paredes, A. Jahanshahi, K. L. Kozielski, *Brain stimul.* **2021**, *14*, 1285.
[2] E. Zhang, M. Abdel-Mottaleb, P. Liang, B. Navarrete, Y. A. Yildirim, M. A. Campos, I. Smith, P. Wang, B. Yildirim, L. Yang, S. Chen, I. Smith, G. Lur, T. Nguyen, X. Jin, B. R. Noga, P. Ganzer, S. Khizroev, *Brain stimul.* **2022**, *15*, 1451.
[3] Y. Zhang, X. Wu, J. Ding, B. Su, Z. Chen, Z. Xiao, C. Wu, D. Wei, J. Sun, F. Luo, H. Yin, H. Fan, *ACS Nano* **2023**, *17*, 15796.
[4] R. P. Narayanan, F. R. Rostami, A. Khaleghi, I. Balasingham, in *2022 IEEE-EMBS International Conference on Wearable and Implantable Body Sensor Networks (BSN)*, IEEE, Piscataway, NJ **2022**, pp. 1–4.
[5] K. L. Kozielski, A. Jahanshahi, H. B. Gilbert, Y. Yu, Ö. Erin, D. Francisco, F. Alosaimi, Y. Temel, M. Sitti, *Sci. Adv.* **2021**, *7*, 3.
[6] C.-W. Nan, M. I. Bichurin, S. Dong, D. Viehland, G. Srinivasan, *J. Appl. Phys.* **2008**, *103*, 3.
[7] M. I. Bichurin, V. M. Petrov, G. Srinivasan, *Phys. Rev. B* **2003**, *68*, 5.
[8] M. M. Vopson, *Crit. Rev. Solid State Mater. Sci.* **2015**, *40*, 223.
[9] S. Kopyl, R. Surmenev, M. Surmeneva, Y. Fetisov, A. Kholkin, *Mater. Today Bio.* **2021**, *12*, 100149.
[10] T. R. Nizamov, A. A. Amirov, T. O. Kuznetsova, I. V. Dorofievich, I. G. Bordyuzhin, D. G. Zhukov, A. V. Ivanova, A. N. Gabashvili, N. Y. Tabachkova, A. A. Tepanov, I. V. Shchetinin, M. A. Abakumov, A. G. Savchenko, A. G. Majouga, *Nanomaterials (Basel, Switzerland)* **2023**, *13*, 5.
[11] F. Alosaimi, D. Dominguez-Paredes, R. Knoben, F. Almasabi, S. Hescham, K. Kozielski, Y. Temel, A. Jahanshahi, *Behav. Brain Res.* **2023**, *444*, 114363.
[12] A. Kargol, L. Malkinski, G. Caruntu, *Adv. Magn. Mater.* **2012**, 89, https://doi.org/10.5772/39100.
[13] E. W. Lee, *Rep. Prog. Phys.* **1955**, *18*, 184.
[14] B. Völker, P. Marton, C. Elsässer, M. Kamlah, *Continuum Mech. Thermodyn.* **2011**, *23*, 435.
[15] A. V. Raut, R. S. Barkule, D. R. Shengule, K. M. Jadhav, *J. Magn. Magn. Mater.* **2014**, *358-359*, 87.
[16] Y. H. Hou, Y. J. Zhao, Z. W. Liu, H. Y. Yu, X. C. Zhong, W. Q. Qiu, D. C. Zeng, L. S. Wen, *J. Phys. D: Appl. Phys.* **2010**, *43*, 445003.
[17] G. A. Sawatzky, F. van der Woude, A. H. Morrish, *J. Appl. Phys.* **1968**, *39*, 1204.
[18] M. Ounacer, A. Essoumhi, M. Sajieddine, A. Razouk, A. Fnidiki, F. Richomme, J. Juraszek, S. M. Dubiel, M. Sahlaoui, *J. Phys. Chem. Solids* **2021**, *148*, 109687.
[19] M. Cococcioni, S. De Gironcoli, *Phys. Rev. B* **2005**, *71*, 035105.
[20] H. J. Kulik, N. Marzari, *J. Chem. Phys.* **2010**, *133*, 11.
[21] D. Fritsch, C. Ederer, *Phys. Rev. B* **2010**, *82*, 10.
[22] A. D. Corso, 'scf_elastic_constants', https://people.sissa.it/~dalcorso/thermo_pw/user_guide22.html (accessed: August 2023).
[23] M. Islam, A. A. Hossain, M. Ahsan, M. Bally, M. S. Ullah, S. Hoque, F. Khan, *RSC Adv.* **2022**, *12*, 8502.
[24] S. Tinte, M. G. Stachiotti, C. O. Rodriguez, D. L. Novikov, N. E. Christensen, *Phys. Rev. B* **1998**, *58*, 11959.
[25] L. Feng-Ying, J. Chang-Qing, Y. Shu-Jie, X. Chang-Jiang, Y. Ri-Cheng, W. Xiao-Hui, L. Jing, L. Xiao-Dong, L. Yan-Chun, C. Liang-Chen, *Chin. Phys. Lett.* **2006**, *23*, 1249.
[26] J. I. Morgan, T. Curran, *Nature* **1986**, *322*, 552.
[27] R. S. Turtelli, M. Kriegisch, M. Atif, R. Grössinger, in *IOP Conference Series: Materials Science and Engineering*, volume *60*, IOP Publishing, Bristol **2014**, p. 012020.
[28] W. Nolting, A. Ramakanth, *Quantum theory of magnetism*, Springer Science & Business Media, Berlin **2009**.
[29] R. Bozorth, E. F. Tilden, A. J. Williams, *Phys. Rev.* **1955**, *99*, 1788.
[30] M. Fiebig, *J. Phys. D: Appl. Phys.* **2005**, *38*, R123.
[31] D. Bilc, R. Orlando, R. Shaltaf, G.-M. Rignanese, J. Íñiguez, P. Ghosez, *Phys. Rev. B* **2008**, *77*, 165107.
[32] Z. Li, S.-K. Chan, M. Grimsditch, E. Zouboulis, *J. Appl. Phys.* **1991**, *70*, 7327.
[33] C. M. Landis, R. M. McMeeking, *Ferroelectrics* **2001**, *255*, 13.
[34] M. Vopson, Y. Fetisov, G. Caruntu, G. Srinivasan, *Materials* **2017**, *10*, 963.
[35] A. Singer, S. Dutta, E. Lewis, Z. Chen, J. C. Chen, N. Verma, B. Avants, A. K. Feldman, J. O'Malley, M. Beierlein, C. Kemere, J. T. Robinson, *Neuron* **2020**, *107*, 631.

© 2024 The Authors. Advanced Healthcare Materials published by Wiley-VCH GmbH

[36] I. Bok, I. Haber, X. Qu, A. Hai, *Sci. Rep.* **2022**, *12*, 8386.
[37] S. O. Estrada, C. A. Huerta-Aguilar, T. Pandiyan, M. Corea, I. A. Reyes-Domínguez, G. Tavizon, *J. Alloys Compd.* **2017**, *695*, 2706.
[38] F. Rattay, *Neuroscience* **1999**, *89*, 335.
[39] R. Cubo, A. Medvedev, M. Åström, *IEEE Design Test* **2016**, *33*, 74.
[40] M. Åström, E. Diczfalusy, H. Martens, K. Wårdell, *IEEE Trans. Biomed. Eng.* **2014**, *62*, 664.
[41] S. W. Lee, F. Fallegger, B. D. Casse, S. I. Fried, *Sci. Adv.* **2016**, *2*, e1600889.
[42] A. S. Aberra, B. Wang, W. M. Grill, A. V. Peterchev, *Brain stimul.* **2020**, *13*, 175.
[43] E. N. Warman, W. M. Grill, D. Durand, *IEEE Trans. Biomed. Eng.* **1992**, *39*, 1244.
[44] B. Wang, W. M. Grill, A. V. Peterchev, *Biophys. J.* **2018**, *115*, 95.
[45] J. B. Ranck Jr, *Brain Res.* **1975**, *98*, 417.
[46] P. Maccabee, V. Amassian, L. Eberle, R. Cracco, *J. Physiol.* **1993**, *460*, 201.
[47] B. D. Goodwin, C. R. Butson, *Neuromodulation: Tech. Neural Interface* **2015**, *18*, 694.
[48] M. Åström, E. Diczfalusy, H. Martens, K. Wårdell, *IEEE Trans. Biomed. Eng.* **2014**, *62*, 664.
[49] F. Rattay, *IEEE Trans. Biomed. Eng.* **1986**, *33*, 974.
[50] J. D. Bronzino, *Biomedical engineering handbook*, vol. *2*, CRC press, Boca Raton **1999**.
[51] G. Bonmassar, S. W. Lee, D. K. Freeman, M. Polasek, S. I. Fried, J. T. Gale, *Nat. Commun.* **2012**, *3*, 921.
[52] S. W. Lee, K. Thyagarajan, S. I. Fried, *IEEE Trans. Biomed. Eng.* **2018**, *66*, 1680.
[53] J. Buhlmann, L. Hofmann, P. A. Tass, C. Hauptmann, *Front. Neuroeng.* **2011**, *4*, 15.
[54] J. T. Francis, B. J. Gluckman, S. J. Schiff, *J. Neurosci.* **2003**, *23*, 7255.
[55] V. Corral-Flores, D. Bueno-Baques, R. d. Ziolo, *Acta Mater.* **2010**, *58*, 764.
[56] P. Giannozzi, S. Baroni, N. Bonini, M. Calandra, R. Car, C. Cavazzoni, D. Ceresoli, G. L. Chiarotti, M. Cococcioni, I. Dabo, A. Dal Corso, S. de Gironcoli, S. Fabris, G. Fratesi, R. Gebauer, U. Gerstmann, C. Gougoussis, A. Kokalj, M. Lazzeri, L. Martin-Samos, N. Marzari, F. Mauri, R. Mazzarello, S. Paolini, A. Pasquarello, L. Paulatto, C. Sbraccia, S. Scandolo, G. Sclauzero, A. P. Seitsonen, et al., *J. Phys.: Condens. Matter* **2009**, *21*, 395502.
[57] P. Giannozzi, O. Andreussi, T. Brumme, O. Bunau, M. B. Nardelli, M. Calandra, R. Car, C. Cavazzoni, D. Ceresoli, M. Cococcioni, N. Colonna, I. Carnimeo, A. Dal Corso, S. de Gironcoli, P. Delugas, R. A. DiStasio Jr, A. Ferretti, A. Floris, G. Fratesi, G. Fugallo, R. Gebauer, U. Gerstmann, F. Giustino, T. Gorni, J. Jia, M. Kawamura, H.-Y. Ko, A. Kokalj, E. Küçükbenli, M. Lazzeri, et al., *J. Phys.: Condens. Matter* **2017**, *29*, 465901.
[58] K. F. Garrity, J. W. Bennett, K. M. Rabe, D. Vanderbilt, *Comput. Mater. Sci.* **2014**, *81*, 446.
[59] A. D. Corso, Github:dalcorso/thermo_pw: Thermo_pw quantum-espresso routines for the automatic computation of ab-initio material properties, https://github.com/dalcorso/thermo_pw (accessed: August 2023).
[60] K. M. Rabe, C. H. Ahn, J.-M. Triscone, in *Topics in Applied Physics*, Springer, Heidelberg, Berlin **2007**.
[61] R. Resta, D. Vanderbilt, *Physics of Ferroelectrics* **2007**, *105*, 31.
[62] A. Dal Corso, *Comput. Mater. Sci.* **2014**, *95*, 337.

© 2024 The Authors. Advanced Healthcare Materials published by Wiley-VCH GmbH